

High Frequency Breast Imaging: Experimental Analysis of Tissue Phantoms

DUY HAI NGUYEN¹, JONATHAN STINDL¹, TERESA SLANINA¹, JOCHEN MOLL¹ (Member, IEEE),
VIKTOR KROZER¹ (Senior Member, IEEE), AND GERNOT ZIMMER²

¹Department of Physics, Goethe University Frankfurt, 60438 Frankfurt, Germany

²Faculty of Computer Science and Engineering, Frankfurt University of Applied Sciences, 60318 Frankfurt, Germany

CORRESPONDING AUTHOR: D. H. NGUYEN (e-mail: nguyen@physik.uni-frankfurt.de)

This work was supported by the Project IndiThera through the Federal Ministry of Education and Research (BMBF) under Grant 13GW0361D.

ABSTRACT This article presents the experimental proof of concept of high-frequency microwave breast imaging system operating from 16 to 20 GHz. At those frequencies the wavelengths are in the order of millimeter range which support better resolution in localizing cancerous tumors compared to the conventional microwave imaging systems. A new antenna is developed with a compact size of $7 \times 7 \text{ mm}^2$, which relies on an ultra-wideband, planar bowtie-like antenna structure. Practical results show that a bandwidth of 23.45 GHz is achieved (16 – 40 GHz) for a reflection loss higher than 10 dB. Furthermore, artificial breast tissue models based on glycerol–oil mixture with agar powder are developed. Dielectric properties of the tissue are stable over a wide frequency range up to 20 GHz at room temperature. The typical high microwave power losses within biological tissue at the operating frequency range are addressed by contacting the antennas directly to the tissue and slightly compressing the phantom without any coupling medium. Hence, the compressed breast geometry has a flat surface with well-defined boundaries, which simplifies tumor localization algorithms. For the purpose of demonstrating the current stage of research, a one-dimensional scanning system is used to localize the tumor's positions inside the simulated, heterogeneous breast model of 36 mm thickness. Using the root mean square deviation algorithm, we can accurately detect positions of the tumors, which have a cross-sectional area down to $4 \times 4 \text{ mm}^2$. The preliminary results show the feasibility of achieving a high resolution with a compact microwave system for early-stage breast cancer detection.

INDEX TERMS Ultra-wideband antenna (UWB), bow-tie structure, heterogeneous breast tissue mimic, root mean square deviation (RMSD) algorithm.

I. INTRODUCTION

BREAST screenings have a crucial impact on detecting cancerous tumors, providing information for proper treatment to improve the survival rate in women [1]. Currently, X-ray mammography, ultrasonography (ultrasound), and magnetic resonance imaging (MRI) are the three most common techniques used in the screening processes [2]. Beside their benefits, there are still, however, limitations with the methods. For example, mammography exposes ionizing radiation, which is harmful for the biological tissue. Moreover, the successful rates of tumor detection in dense breasts are significantly degraded [3]. Ultrasound is

an effective method with low cost, but its results considerably depend on the execution and experience of the operators [4]. MRI has the advantage of facilitating excellent resolution of the breast image. However, it is too expensive for common usages in screenings [5]. Since microwave technology has advantages in breast imaging regarding the above-mentioned points, it is an attractive method as a replacement or complement modality to the current approaches. In fact, microwave signals propagate in biological tissue without ionization and achieve broadband operation with high-resolution images of the breast. In addition, current microwave technology is capable of achieving cost-effective, compact, and fully

automated systems, which can be widely used, minimizing human failure during the process.

Over decades, numerous studies have been reported about microwave breast imaging techniques [6]–[10]. Most of these systems have similarities in both hardware infrastructure and image reconstruction algorithms. For example, ultra-wideband (UWB) antennas are adopted to cover a wide frequency spectrum up to 10.6 GHz, which compromises a trade-off between power losses and penetration capability of the microwave signals inside the biological tissue [2]. Coupling media, such as saline or glycerol solutions [6], [11], can reduce mismatches at the antenna–skin interface, and thus enhance transmission between the antennas. Furthermore, breast structures are usually visualized in two- or three-dimensional images by typical tomography or radar-based analyses, such as the Gauss-Newton method [12], delay and sum (DAS) [13], or microwave space-time beamformer (MIST) [14].

This paper investigates the transmission capability of microwave signals from 16 to 20 GHz through artificial breast tissue and the localization ability of inserted tumorous tissue. We propose a new ultra-wideband (UWB) patch, bowtie-like antenna structure, which has a practical bandwidth of 23.45 GHz for reflection coefficient lower than -10 dB. The antenna has direct contact with the skin without any coupling medium by means of breast compression. This approach reduces reflection at the antenna–skin interface, transmission losses from the coupling medium, and the diffraction limit [15]. Therefore, more power can penetrate the tissue at the defined bandwidth. On top of this, we have also developed artificial breast tissue models based on agar, glycerol, and oil mixture [16]. The dielectric properties of the models have a good agreement with theoretical values [17], [18] over a wide frequency range (up to 20 GHz). For demonstrational purposes in laboratory conditions, we introduce a one-dimensional (1D) scanning system to detect cancerous tumors. The preliminary results show that based on a simple root mean square deviation (RMSD) algorithm [19], a small-sized tumor with a cross-section of $4 \times 4 \text{ mm}^2$ is localized accurately inside a heterogeneous breast tissue model with a thickness of 36 mm.

The rest of this article is organized as follows. In the first two sections, we introduce the design of the proposed antenna, and the development of artificial breast tissue. The following section will then present the algorithms to detect tumor’s positions. The fifth section will describe the 1D scanning system. Finally, further discussions and conclusions will be presented in Sections VI and VII, respectively.

II. ANTENNA STRUCTURE

An overview of the antenna structure is shown in Fig. 1. Here, a multi-layer technology allows the integration of a radiating element and its excitation network on the same substrate (Rogers RO4350B, $\epsilon_r = 3.55$ at 10 GHz [20]). This results in a compact and lightweight structure. As can be seen in the figure, four conducting layers are employed for

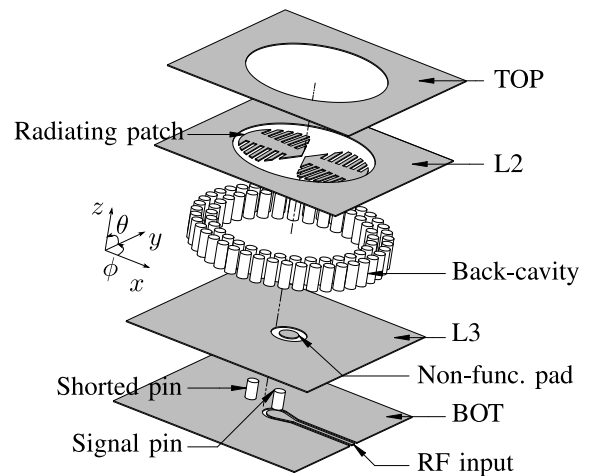


FIGURE 1. Overview of the antenna structure with multi-layer technology. Substrate is not shown for simplicity.

the radiating element (TOP–L3) as well as its power distribution network (L3–BOT). Both structures share a common ground layer L3, which improves signal isolation between them. The substrate thickness of the antenna and its input is about $h_{antenna} = 0.91 \text{ mm}$ and $h_{feed} = 0.31 \text{ mm}$, respectively. As reported in the previous studies [21], microwave signals at high frequency ranges suffer from significant power loss inside biological tissue. For this reason, main radiators are designed at L2 with a clear aperture from TOP layer to preserve the antenna’s characteristics before propagating to the tissue. A bowtie-like antenna is realized by deploying two radiating patches, excited by a transmission pin from BOT layer. From the figure, an unbalanced excitation method is adopted in the design by short-circuiting one radiating arm (left) to minimize the structure dimensions. The pin’s diameter is $\varnothing_{pin} = 0.4 \text{ mm}$, which requires non-functional pads in each layer to properly establish a signal path, according to the manufacturer’s rules. Furthermore, we also use ground via holes to form a metallic back-cavity, which helps to reduce mutual coupling between elements in planar structures caused by surface wave propagation [22]. As a result, impedance bandwidth and radiation characteristics are significantly improved [23].

In this study, our proposed on-body antenna has direct contact to the biological tissue by means of compression. Hence, power loss reduction is expected due to the minimization of mismatches at the interface or coupling medium and the tissues or antenna, respectively. A simulation setup in CST Microwave Studio for a single antenna is depicted in Fig. 2. According to the figure, a simplified, heterogeneous breast tissue model composes of skin and fat layers, which have thicknesses of $h_{skin} = 1.5 \text{ mm}$ and $h_{fat} = 10 \text{ mm}$, respectively. Open boundary conditions are applied at the breast tissue’s sides for perfect signal absorption. Furthermore, a free space surrounds the antenna to mimics a realistic environment when characterizing the element in later steps. Our previous study [24] showed that

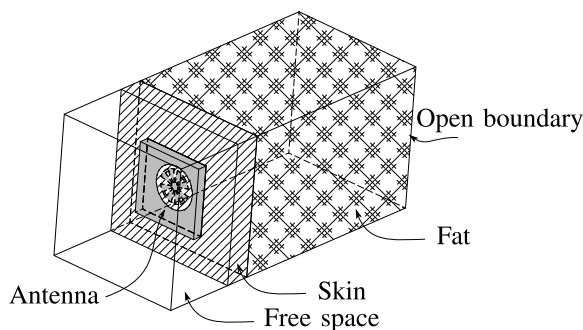


FIGURE 2. Simulation setup for the antenna design. Open boundary conditions are applied at the tissue’s surface to ensure no reflected power to the antenna.

TABLE 1. Parameter values of the one-pole Cole–Cole expression for different breast tissues in *ex vivo* conditions [18].

| Tissue | ϵ_∞ | $\Delta\epsilon$ | τ (ps) | α | σ_s (S/m) |
|--------|-------------------|------------------|-------------|----------|------------------|
| Fat | 4 | 6 | 10 | 0.09 | 0.1 |
| Skin | 6 | 36.5 | 9.4 | 0.06 | 0.7 |
| Tumor | 5 | 50.5 | 9 | 0.07 | 0.9 |

the simple, two-layer biological tissue model, as shown in the Fig. 2, offers a good agreement between simulations and measurements while maintaining low computation complexity.

Complex dielectric properties of the tissue for the simulation are deduced by the one-pole Cole–Cole model, [17], [18], which is expressed in Eq. (1) as:

$$\epsilon(\omega) = \epsilon'(\omega) - j\epsilon''(\omega) = \epsilon_\infty + \frac{\Delta\epsilon}{1 + (j\omega\tau)^{1-\alpha}} + \frac{\sigma_s}{j\omega\epsilon_0} \quad (1)$$

The complex permittivity $\epsilon(\omega)$ is approximated by the experimental data with fitting terms: τ – relaxation time of material, which defines the relaxation frequency $f_{relax} = \frac{1}{2\pi\tau}$, ϵ_∞ – dielectric constant of material well above the relaxation frequency, $\Delta\epsilon = \epsilon_\infty - \epsilon_s$ – the difference between the infinite and static dielectric constant, which is well below the relaxation frequency, σ_s – static conductivity, $0 \leq \alpha \leq 1$ and $\epsilon_0 = 8.85 \times 10^{-12}$ F/m. The fitting values for some typical breast tissues are listed in Table 1 [18], and they are graphically illustrated as in Fig. 6.

Photographs of the realized antenna are shown in Fig. 3, and its input reflection is acquired by a vector network analyzer (VNA). The measurement is conducted on the breast of a female volunteer and the advanced NIST multi-line calibration [25] is used. With the chosen calibration, a same reference plane between the experimental and simulated results is achieved, and thus they are suitable for a direct comparison, as depicted in Fig. 4. According to the figure, the measurement corresponds to the simulation, and the impedance bandwidth is from 16.55 to 40 GHz for a reflection coefficient lower than -10 dB. Some additional peaks are observed in the measurement, which might come from the manufacturing tolerances, for instance misalignments between the conducting layers, or the deviation of the practical dielectric constant from materials.

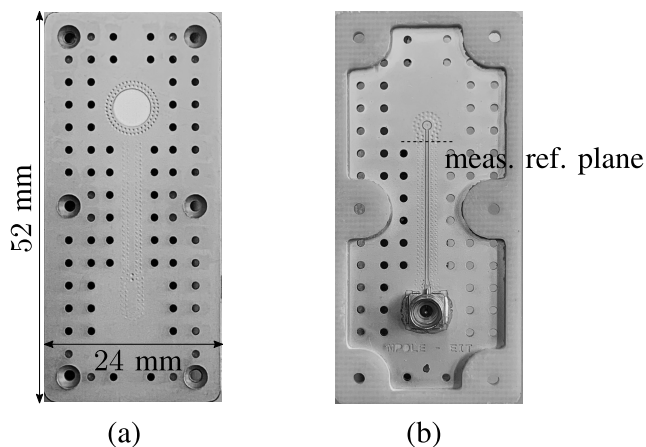


FIGURE 3. Photographs of the bowtie antenna prototype. (a) Top view. (b) Bottom view.

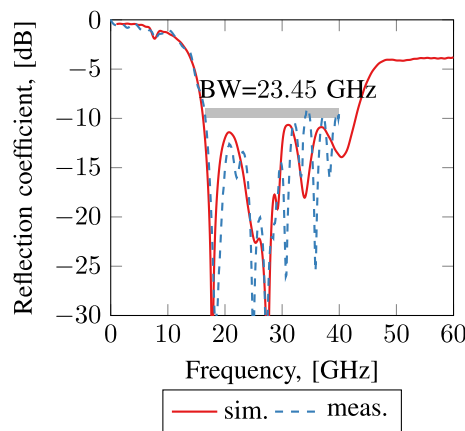


FIGURE 4. Measured reflection coefficient of the antenna. The results are obtained by placing the antenna in direct contact with the breast of a female volunteer.

TABLE 2. Material list for mimicking different breast tissue models.

| Tissue | Distilled water (ml) | Glycerol (ml) | Agar (gram) | Rapeseed oil (ml) | Dishwashing liquid (ml) |
|--------|----------------------|---------------|-------------|-------------------|-------------------------|
| Tumor | 50 | 10 | 5.5 | 15 | 4 |
| Skin | 55 | 17.5 | 6.8 | 50 | 3 |
| Fat | 35 | 35 | 6.8 | 100 | 3 |

III. BIOLOGICAL BREAST TISSUE MODELS

Artificial models are commonly used to substitute real breast in preliminary laboratory investigations. Hence, it is important to have a simple development procedure while the models maintain accurate dielectric properties over the frequency range of interest. There have been numerous studies in the literature, which proposed different kinds of breast tissues in both liquid and solid forms [26]–[29]. To gain flexibility in evaluating our microwave system, semi-solid breast tissue, based on agar–oil mixture, are investigated and developed in this work. Table 2 summaries a material list to mimic different breast tissue type. The development process is as follows.

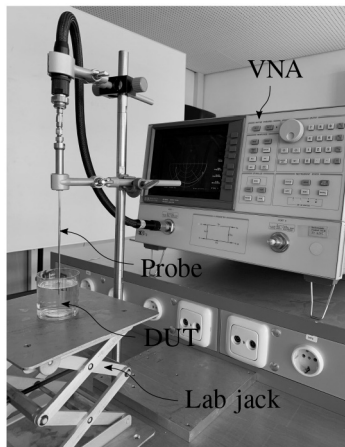


FIGURE 5. Measurement setup to characterize breast tissue models using open-ended, coaxial probe method.

- The agar powder (Sigma-Aldrich A1296) is added into a glycerol (Sigma-Aldrich G5516)–water solution, and the mixture is slowly heated up to 63 °C by a magnetic stirrer.
- The rapeseed oil (Rewe Ja Rapsöl) is preheated to a minimum temperature of 60 °C during the stirring process.
- The agar mixture is mixed slowly with the rapeseed oil. During the process, the temperature should not be lower than 50 °C.
- After that, the dishwashing liquid (Fairy Ultra Konzentrat Handspülmittel) is added. The slow stirring is continued until the mixture becomes a uniform, dense liquid. As the mixture becomes thickened, manual stirring by hand is also required.
- The final mixture is filled in a mold and rests for at least 12 hours before use.

In comparison to mimicked breast tissue based on gelatin, the use of agar powder results in harder mixture, which possesses better mechanical characteristics. Moreover, a glycerol–water solution is adopted to reduce the natural evaporation process of water. Thereby dielectric properties are stabilized regarding temperature fluctuations. Complex permittivities of the artificial tissue models are characterized by the open-ended, coaxial probe technique [30], which is illustrated in Fig. 5. Here, a slim probe and a software package from Keysight [31] are used to calculate the dielectric properties of the material from the S -parameters. An adjustable laboratory jack ensures a tight contact between the tissue’s surface and the probe’s terminal for accurate measurement results. The deduced complex permittivities of the models are compared to Cole–Cole expressions for the breast tissue in an *ex vivo* condition [17], [18], which are depicted in Fig. 6. According to the results, the dielectric properties of the simulated breast tissue are similar to the theoretical values. In addition, regarding the figure, deviations in the measured dielectric properties of the fat tissue to the mathematical

model is observed. An adjusted Cole–Cole expression for the measured fat values from Table 1 is conducted by new relaxation time $\tau = 40$ ps and dielectric difference $\Delta\epsilon = 10$. Therefore, the substance’s ratio (e.g., glycerol–water solution) for the fat tissue model is not yet optimized. However, within the interested frequency range ([16, 20] GHz), the simulated tissue are capable for the study. Furthermore, an important remark from the Cole–Cole expressions is that they are average values based on measurements of volunteers from different age groups and physical statuses. Hence, although there are still some deviations between practical and theoretical values, the properties of the mimicked tissue are sufficiently accurate and suitable for further experiments.

IV. IMAGE RECONSTRUCTION ALGORITHMS

A. TIME DOMAIN TRANSFORMATION

By using time domain signals for the analysis, one can select a time range of interest, which corresponds to a certain signal propagation delay. This is closely related to time domain gating, which is used to remove unwanted reflections during the analysis of electronic networks [32]. For this reason, inverse fast Fourier transformation (IFFT) is used to transform the acquired S -parameters from frequency to time domain values. Theoretically, an ideal signal for the standard IFFT includes an equally spaced (Δ_f), symmetrical frequency spectrum about the DC component (i.e., 0 Hz) [33], as shown in Fig. 7(a). However, the measured S -parameters from the VNA are practically in a defined frequency range lacking a negative spectrum and DC component, visualized as the solid area in Fig. 7(b). Therefore, three common IFFT adjustments are used to address the problem: (i) unshifted lowpass transformation (uLPT), (ii) shifted lowpass transformation (sLPT), and (iii) bandpass transformation (BPT) [34].

For the lowpass transformation, a DC component and the complex conjugate of the mirrored S -parameter representing the negative frequency samples are added to the measured data [34]. This results in a frequency signal having an even real part and an odd imaginary part. This is termed hermitian and provides a real time domain representation after calculation of the IFFT [32]. This method is visualized in Fig. 7(b) using a solid line for the positive frequency range and a dashed line for the added negative frequency data. In the figure, the frequency difference between the DC component and starting frequency is expressed by $M\Delta_f$, with M being an integer number. If M equals one, the method is called unshifted lowpass transformation (uLPT). Thus, uLPT causes a frequency mismatch of $f_{\text{shift}} = f_{\text{start}} - \Delta_f$ as the starting frequency is usually larger than the frequency spacing. If f_{start} is a multiple of Δ_f , M can be chosen to match the starting frequency, i.e., $M\Delta_f = f_{\text{start}}$, by adding zeros as samples between DC component and starting frequency. The application of the IFFT to this arrangement is known as shifted lowpass transformation (sLPT) [34]. However, the sLPT can be calculated even if f_{start} is not a multiple of Δ_f by considering the mathematical frequency mismatch which

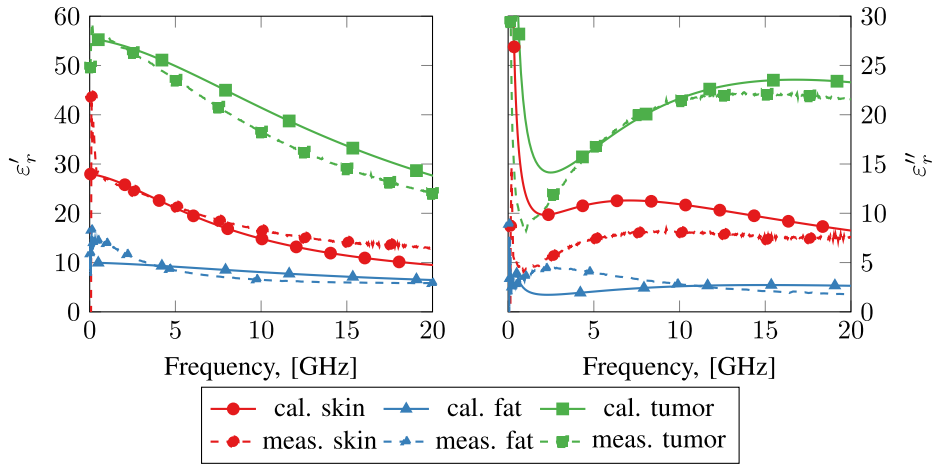


FIGURE 6. Dielectric properties of the breast tissue. Calculated values in solid lines (e.g., cal. skin) are referred from Martellosio's work [18]. Measured values in dashed lines (e.g., meas. skin) are practical dielectric properties of the mimicked tissues used in the demonstration system.

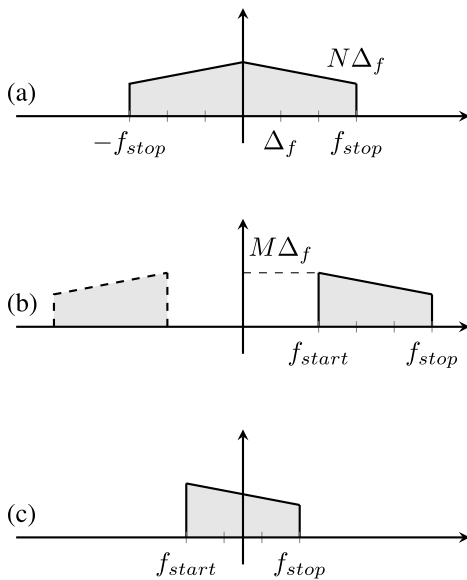


FIGURE 7. Inverse fast Fourier transformation types. (a) Standard transformation. (b) Lowpass transformation (c) Bandpass transformation.

leads to Eq. (2) [34]:

$$e_{shift}(t) = e_1(t)e^{2i\pi f_{shift}t} + e_1^*(t)e^{-2i\pi f_{shift}t} \quad (2)$$

In the equation, $e_1(t)$ is the result of the IFFT applied to a similar data structure as for the uLPT with the difference that the values corresponding to negative frequency values are zeroed, and $e_1^*(t)$ is the complex conjugate of the $e_1(t)$. Outcomes of Eq. (2) are real values because the second term of the formula is the complex conjugate of the first one. On contrary to the lowpass transformations, the BPT can be calculated without adding data to the measured frequency values by applying the IFFT directly, which is ordered in a way that the center of the frequency data is assigned to DC component, as shown in Fig. 7(c) [34]. A drawback is that the frequency mismatch of this method is even higher than of the uLPT because half of the data is shifted to the negative

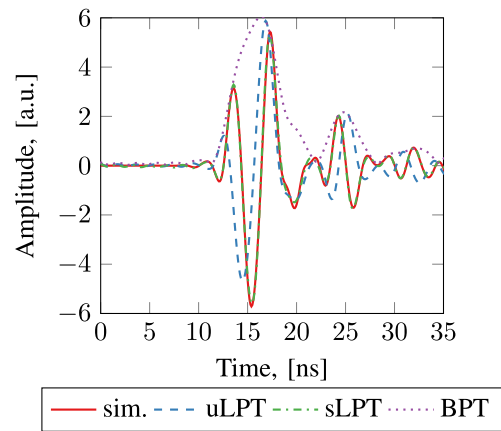


FIGURE 8. Comparison of time signals created with different transformations to time domain. Reference signal (sim.) in time domain is generated by impulse response from the simulator. Frequency response of the reference signal is used to evaluate the different Fourier transformations.

spectrum. Since the modified data arrangement is not hermitian, the IFFT results are complex numbers. Therefore, absolute values are used to represent the transformed time signals of the BPT approach.

A comparison of time signals using the different transformations is shown in Fig. 8. According to the figure, sLPT shows an excellent agreement with the reference signal due to the correction of the frequency mismatch. As expected, the uLPT also reproduces a similar waveform but with a shift in the whole spectrum. Furthermore, the result of the BPT is quite different and behaves like an envelope for both LPT methods. Thus, in this work, the measured S -parameters are transformed to time domain by using the sLPT as it generates the closest approximation to the reference. Moreover, a Hanning window is applied to the measured data before the IFFT to avoid any sidelobes.

B. TUMOR LOCALIZATION

Similar to mammography, the breast compression does not only reduce the power losses at high frequency ranges but

also simplifies the breast geometry. Therefore, localization of the cancerous tissue in a 1D scan is conducted based on the root mean square calculation (RMS) [19]:

$$RMS(x_i) = \sqrt{\frac{1}{n} \sum_{i=1}^n (s(x_i, t_i))^2} \quad (3)$$

In this equation, n is the number of time domain samples. Moreover, $s(x_i, t_i)$ is the signal value of position x_i and at the instantaneous time t_i , respectively. Signals, which have the same average amplitudes, produce larger RMS values if there are high amplitudes at some moments in time t_i . On the contrary, the RMS is lowest when the amplitudes are identical for the entire period. If there is a reference signal, deviations between the actual and reference data can help to eliminate the influences of the measurement setup. The reference is usually made by measuring a similar breast model in the same setup but without any cancerous tumors, which is also known as a baseline. In this case, taking RMS of the difference is also referred to as the root mean square deviation (RMSD), which generally shows the tumor's locations more clearly. The RMSD is defined as follows:

$$RMSD(x_i) = \sqrt{\frac{1}{n} \sum_{i=1}^n (s_0(x_i, t_i) - s(x_i, t_i))^2} \quad (4)$$

where n is the total number of time samples, $s_0(x_i, t_i)$ and $s(x_i, t_i)$ are the baseline and the actual measured values, respectively.

V. EXPERIMENTAL DEMONSTRATION

A. MEASUREMENT SETUP

The transmission capability of the proposed antenna through biological tissue is demonstrated by a 1D scanning system, which is depicted in Fig. 9. Regarding the figure, transmitting and receiving antennas (Fig. 3), i.e., Tx–Rx, are mounted on the metal frame of the scanning axes, and their apertures are directly opposite of each other. The antennas are adjusted to compress the breast tissue model to reduce the air gap between their interfaces, and the thickness of the tissue is about 36 mm. To improve the detectability of the signals transmitted through the breast model, a low-noise amplifier (LNA) is adopted at the receiving antenna. The LNA features a bandwidth from 10 to 30 GHz (return loss $RL \geq 10$ dB) with an excellent noise figure of $NF = 1.35$ at room temperature [35]. A two-port VNA (HP8720C) is used to excite the transmitting antenna at 10 dBm input power and to receive the detected output power from the LNA. Also, the RMS algorithm is based on difference between the current measurement and its reference, which is also acquired in the similar condition. Hence, the S -parameters from the VNA are raw values without any calibrations. Within the interested frequency range, excluding losses from the connectors and cables, a practical excitation power at the antenna is approximately 7.2 dBm. In addition, the operational frequency is set from 16 to 20 GHz (maximum

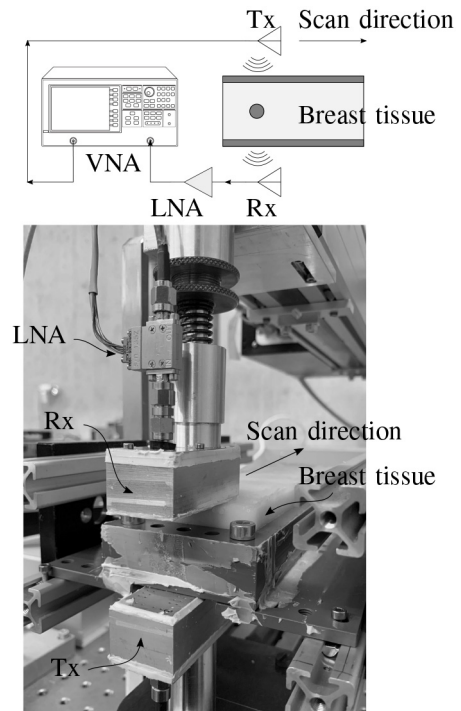


FIGURE 9. A schematic view of the 1D scanning system.

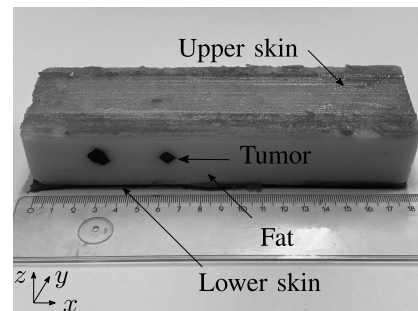


FIGURE 10. Overview of the heterogeneous breast tissue model. The breast phantom includes skin and fat layers with thicknesses of 2 and 32 mm, respectively. Two silicon cancerous tumors with different dimensions are also used.

range of the VNA) to use the antennas just within their bandwidth.

Fig. 10 shows a simple, heterogeneous breast tissue, consisting of skin, fat layers, and cancerous tumors. The tissue models are developed and characterized as mentioned in the previous Section III. The practical dielectric properties of the tissues are also shown in Fig. 6. The upper and lower skin layers are approximately 4 mm thick. During the scanning process a practical thickness of 2 mm is observed. The fat layer is about 32 mm, which results in the total dimension of $178 \times 50 \times 36$ mm ($l \times w \times h$). Also from the figure, two cancerous tumors in cylindrical and cuboid shape, are located within the first half of the tissue phantom at $z_1 = z_2 = 13$ mm, $x_1 = 32$ mm, and $x_2 = 64$ mm, respectively. The cylinder has a diameter of 8 mm, while the other tumor has a cross-sectional area of 4×4 mm².

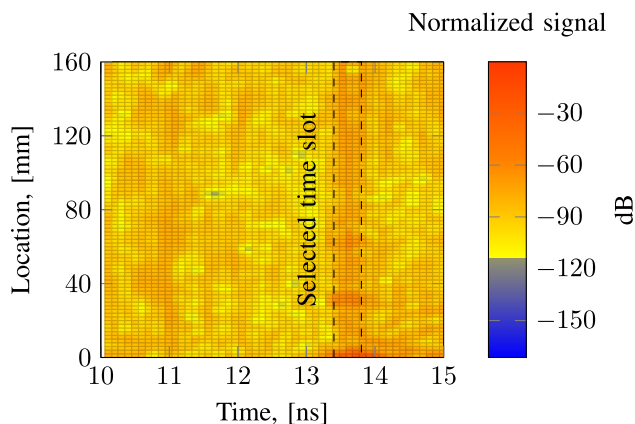


FIGURE 11. Time-position matrix of the scanning results, generated by sLPT and zero-padding to the missing frequency samples. The time range from 10 to 15 ns is shown as the maximum amplitudes appear within this range.

B. DATA ANALYSIS

A section of the time–position matrix generated with the sLPT of the transmission S -parameter is depicted in Fig. 11. Since maximum amplitudes appear from 13.4 to 14 ns, this time slot is selected for further analysis. Normalized RMS values calculated with the defined time section are shown in Fig. 12. In the figure, four major peaks are observed at positions of 0 mm, 31.5 mm, 63 mm, and 178 mm, respectively. From the measurement setup (Fig. 9), strong reflections at the boundaries (model’s edges and plastic frames) cause two maxima at 0 mm and 178 mm. The other two peaks, highlighted by shaded areas, are due to the appearance of the tumors. In fact, at these positions, different contrasts of the dielectric properties between the tumorous and fat tissue cause changes in the scattering signals. As a consequence, RMS values are higher accordingly. The calculated RMS result of tumor 1 is higher than tumor 2 ($0.35 \geq 0.18$) because of its larger dimension. Taking reference positions in the Fig. 10, our demonstration system exhibits an accurate localization of the tumors. In the second half of the mimicked breast model (from 90 to 178 mm) an average RMS value is also higher than the first half, which might be due to stronger reflection from its edge (178 mm). A minor peak at 150 mm could be considered as a result of the inhomogeneous fat tissue during the development.

As mentioned earlier, taking reference to the baseline signals could theoretically suppress the effects of the measurement’s setup. For this reason, a RMSD calculation is also studied, and the results are shown in Fig. 13. Here, measured data from the first half (with tumors, $x = \{0, 89\}$ mm) are compared to the baseline (without tumors, $x = \{90, 178\}$ mm) in the second half of the structure. According to Fig. 13, three peaks are detected, in which the maximum value at $x = 0$ mm is caused by the measurement setup. Again, the other two peaks at 31.5 mm and 63 mm clearly show the tumors’ positions. In this case, the strong reflection at the boundary cannot be completely discriminated which is probably caused by unequal distances between antenna and

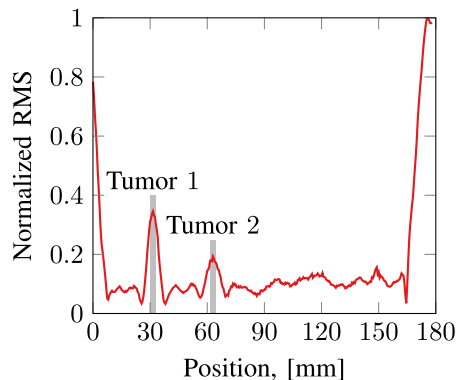


FIGURE 12. RMS calculation of measured data in the selected time slot from 10 to 15 ns, normalizing to the average values of the total measurement. Peaks at 0 and 178 mm appear due to reflection from the holding frame.

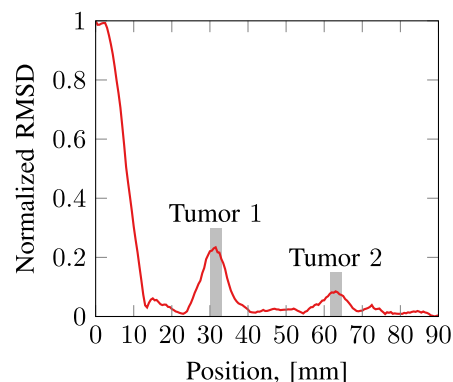


FIGURE 13. RMSD calculation of measured data in the selected time slot from 10 to 15 ns, normalizing to the average values of the total measurement. Measured results from the second half of the phantom (90 to 178 mm) are used as the baseline (without tumors).

edge of the phantom at the beginning and end of the scan. In fact, RMS values at 0 mm and 178 mm in the Fig. 12 differ from each other. Hence, the RMSD method requires a precise measurement setup to be maximum efficient, which is a challenge in practice.

VI. DISCUSSIONS

In this section, we summarize several important points and discuss our observation from this work as follows.

- The proposed antenna has a practical bandwidth of 23.45 GHz up to 40 GHz for a return loss better than 10 dB. Due to availabilities in our laboratory, a 1D scanning system with the antennas is evaluated from 16 to 20 GHz.
- The system scans the sample in a total length of 178 mm with a 1 mm step. Total time requirement for a complete scan is about 15 minutes. Also, repeatability of the method is largely limited by the thin skin layers. Hence, the scan procedure is repeated maximum two or three times for each phantom sample.
- Root mean square (deviation) calculations of the transmission signals (Fig. 12 and Fig. 13), show feasibility to

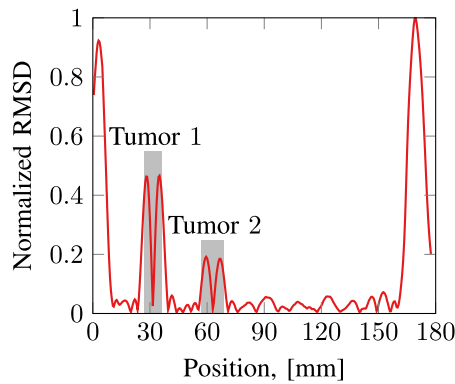


FIGURE 14. Adapted RMSD calculation of measured data, normalizing to the average values of the total measurement. The frequency signals are transformed into time domain values by bandpass transformation. The RMSD calculation is based on referencing neighbour locations.

localize the tumors within a compressed, heterogeneous breast model with a thickness of 36 mm.

- A precise measurement process is needed for the root mean square deviation (RMSD) to effectively eliminate the impacts of the setup. Unfortunately, the requirement is difficult to achieve in practice due to different breast geometries or material compositions.
- As mentioned earlier, the RMS(D) results in the last section are based on the sLPT due to its closest approximation to the ideal signal. However, the method exhibits additional oscillations when the starting frequency is further away from the DC component. The effect is well discussed in the previous study [34]. For localization algorithms based on calculating deviations of the current data to a reference, highly oscillating signals might introduce more errors.
- Implementation of uLPT shows similar results as the sLPT, which are already plotted in the Figs. 12 and 13.
- Requirements of the similar setup between actual and baseline measurements in the conventional RMSD and limitations of the sLPT leads to difficulty to achieve a robust, practical 1D microwave breast imaging system. During our research, we found that bandpass transformation (BPT) works best for this scenario. In addition, values from neighbor positions (before and after) of the considering data point are taken as the reference in the RMSD algorithm. Fig. 14 shows the calculated RMSD based on BPT with RMSD of 10 neighbor positions. According to the figure, the influence of the boundaries still exists, which is represented by two maximum peaks at both ends. However, the adapted method shows clear, distinct peaks corresponding to the tumors' positions, while other areas are well suppressed. In fact, compared to the RMS values in the Fig. 12, higher RMS values and the minor peak at 150 mm in the second half are sufficiently eliminated. By analyzing deviation with surrounding positions, minimum RMSD values are computed at the farthest edge of the tumor's shape from the antennas.

- One important aspect is that we have no coupling media or contrast agent, e.g., gadolinium [5], in this study. In addition, future work will use a larger frequency spectrum supported by the antenna with a static array configuration. Hence, electronic switching mechanism without mechanical movements could significantly reduce data acquisition time.
- Through the antenna footprint of approximately 49 mm² with a corrected power of 5.25 mW, the tissue is exposed by a peak power density of 10.7 mW/cm². According to the Directive 2004/40/EC [36] from the European Commission, the allowed peak power density should not exceed 20 times the value of 5 mW/cm². Thus, the radiated power is harmless to the patients. In addition, the operating frequency range also exhibits non-ionizing radiation to the tissue. Also, for other microwave imaging systems operating in the far-field region, the equivalent plane wave power density for the frequency band from 2 to 300 GHz should not higher than 50 W/m².

VII. CONCLUSION

This article presents a study of transmission capability through biological tissue by using microwave signal propagation from 16 to 20 GHz for early-stage breast cancer detection. This work proposes a wideband patch antenna design which relies on a bowtie structure. Although fabricating on common laminates with low dielectric constant and small loss, the antenna still achieves a wide bandwidth of 23.45 GHz for a reflection coefficient lower than -10 dB. The breast compression by the antennas allows us to reduce losses due to mismatches at the interfaces or through the coupling medium. Thus, more power can be transmitted inside the breast. In addition, artificial breast tissue models based on agar, glycerol, water, and oil mixture are also studied in this paper. Three common breast tissue models (e.g., fat, skin, tumor) are developed and characterized. For the purpose of demonstration, a 1D scanning system experiment is conducted, in which the proposed antenna scans along a compressed, heterogeneous breast model with 178 mm length, and 36 mm height. Two tumors with the smallest edge of 4 mm are accurately detected by using a root mean square algorithm. Furthermore, different inverse fast Fourier transformations and variations of the RMS calculation are discussed. The results show that for our scanning system bandpass transformation (BPT) of frequency signals and root mean square deviation based on neighbor positions provide the most robust results. These preliminary outcomes promise feasibility in developing a compact, simple breast cancer detection system at higher frequency ranges. In the next steps of this study, the detectability limitations of the system will be investigated, such as the maximum thickness of the breast tissue, or the smallest tumor's dimensions. In addition, a better heterogeneous phantom, including different tissue layers, is also used to have more realistic benchmarks. A two-dimensional scanning system will be developed to achieve

a better representation of the tumors, including their shapes and positions inside a heterogeneous breast tissue model. Furthermore, a system with static antenna arrays will be also investigated to make an agile, effective solution instead of scanning procedures, which usually require longer time in operation.

REFERENCES

- [1] H. Sung *et al.*, “Global cancer statistics 2020: GLOBOCAN estimates of incidence and mortality worldwide for 36 cancers in 185 countries,” *CA Cancer J. Clinicians*, vol. 71, no. 3, pp. 209–249, Feb. 2021.
- [2] N. K. Nikolova, “Microwave imaging for breast cancer,” *IEEE Microw. Mag.*, vol. 12, no. 7, pp. 78–94, Dec. 2011.
- [3] J. Kissane, J. A. Neutze, H. Singh, and S. Patel, *Radiology Fundamentals Introduction to Imaging and Technology*, 6th ed. Cham, Switzerland: Springer, 2020.
- [4] A. N. Sencha, E. V. Evseeva, M. S. Mogutov, and Y. N. Patruncov, *Breast Ultrasound*. Berlin, Germany: Springer, 2014.
- [5] R. E. Hendrick, *Breast MRI: Fundamentals and Technical Aspects*. New York, NY, USA: Springer, 2007.
- [6] P. M. Meaney, M. W. Fanning, D. Li, S. P. Poplack, and K. D. Paulsen, “A clinical prototype for active microwave imaging of the breast,” *IEEE Trans. Microw. Theory Tech.*, vol. 48, no. 11, pp. 1841–1853, Nov. 2000.
- [7] E. C. Fear, J. Bourqui, C. Curtis, D. Mew, B. Docktor, and C. Romano, “Microwave breast imaging with a monostatic radar-based system: A study of application to patients,” *IEEE Trans. Microw. Theory Tech.*, vol. 61, no. 5, pp. 2119–2128, May 2013.
- [8] A. W. Preece, I. Craddock, M. Shere, L. Jones, and H. L. Winton, “MARIA M4: Clinical evaluation of a prototype ultrawideband radar scanner for breast cancer detection,” *J. Med. Imag.*, vol. 3, no. 3, Jul. 2016, Art. no. 033502.
- [9] E. Porter, M. Coates, and M. Popović, “An early clinical study of time-domain microwave radar for breast health monitoring,” *IEEE Trans. Biomed. Eng.*, vol. 63, no. 3, pp. 530–539, Mar. 2016.
- [10] H. Song *et al.*, “Detectability of breast tumor by a hand-held impulse-radar detector: Performance evaluation and pilot clinical study,” *Sci. Rep.*, vol. 7, no. 1, Dec. 2017, Art. no. 16353.
- [11] T. M. Grzegorzczak, P. M. Meaney, P. A. Kaufman, R. M. di Florio-Alexander, and K. D. Paulsen, “Fast 3-D tomographic microwave imaging for breast cancer detection,” *IEEE Trans. Med. Imag.*, vol. 31, no. 8, pp. 1584–1592, Aug. 2012.
- [12] J. M. Ortega and W. C. Rheinboldt, *Iterative Solution of Nonlinear Equations in Several Variables* (Classics in Applied Mathematics). Philadelphia, PA, USA: Soc. Ind. Appl. Math., 1970.
- [13] R. Benjamin, “Synthetic, post-reception focusing in near-field radar,” in *Proc. EUREL Int. Conf. Detection Abandoned Land Mines Humanitarian Imperative Seeking Tech. Solution*, 1996, pp. 133–137.
- [14] E. J. Bond, X. Li, S. C. Hagness, and B. D. Van Veen, “Microwave imaging via space-time beamforming for early detection of breast cancer,” *IEEE Trans. Antennas Propag.*, vol. 51, no. 8, pp. 1690–1705, Aug. 2003.
- [15] J. C. Lin, “Frequency optimization for microwave imaging of biological tissues,” *Proc. IEEE*, vol. 73, no. 2, pp. 374–375, Feb. 1985.
- [16] S. Rajagopal, N. Sadhoo, and B. Zeqiri, “Reference characterisation of sound speed and attenuation of the IEC agar-based tissue-mimicking material up to a frequency of 60 MHz,” *Ultrasound Med. Biol.*, vol. 41, no. 1, pp. 317–333, 2015.
- [17] M. Lazebnik *et al.*, “A large-scale study of the ultrawideband microwave dielectric properties of normal, benign and malignant breast tissues obtained from cancer surgeries,” *Phys. Med. Biol.*, vol. 52, no. 20, pp. 6093–6115, 2007.
- [18] A. Martellosio *et al.*, “Dielectric properties characterization from 0.5 to 50 GHz of breast cancer tissues,” *IEEE Trans. Microw. Theory Tech.*, vol. 65, no. 3, pp. 998–1011, Mar. 2017.
- [19] E. Norouzzadeh *et al.*, “Numerical and experimental analysis of a transmission-based breast imaging system: A study of application to patients,” *Int. J. Microw. Wireless Technol.*, vol. 12, no. 6, pp. 469–476, 2020.
- [20] “RO4000® series high frequency circuit materials,” Rogers Corp., Chandler, AZ, USA, Rep. RO 1.4000, 2018. [Online]. Available: <http://www.rogerscorp.com>
- [21] F. Topfer and J. Oberhammer, “Millimeter-wave tissue diagnosis: The most promising fields for medical applications,” *IEEE Microw. Mag.*, vol. 16, no. 4, pp. 97–113, May 2015.
- [22] R. Garg, P. Bhartia, I. J. Bahl, and A. Ittipiboon, *Microstrip Antenna Design Handbook* (Antennas and Propagation Library). Norwood, MA, USA: Artech House, 2001.
- [23] D. H. Nguyen, J. Ala-Laurinaho, J. Moll, V. Krozer, and G. Zimmer, “Improved sidelobe-suppression microstrip patch antenna array by uniform feeding networks,” *IEEE Trans. Antennas Propag.*, vol. 68, no. 11, pp. 7339–7347, Nov. 2020.
- [24] D. H. Nguyen, V. Krozer, J. Moll, and G. Zimmer, “Ultra-wideband on-body elliptical monopole antenna,” *Electron. Lett.*, vol. 57, no. 5, pp. 200–202, Mar. 2021.
- [25] D. F. Williams, C. M. Wang, and U. Arz, “An optimal multiline TRL calibration algorithm,” in *IEEE MTT-S Int. Microw. Symp. Dig.*, vol. 3, 2003, pp. 1819–1822.
- [26] N. Joachimowicz, C. Conessa, T. Henriksson, and B. Duchêne, “Breast phantoms for microwave imaging,” *IEEE Antennas Wireless Propag. Lett.*, vol. 13, pp. 1333–1336, 2014.
- [27] M. Lazebnik, E. L. Madsen, G. R. Frank, and S. C. Hagness, “Tissue-mimicking phantom materials for narrowband and ultrawideband microwave applications,” *Phys. Med. Biol.*, vol. 50, no. 18, pp. 4245–4258, 2005.
- [28] N. Arteaga-Marrero, E. Villa, J. González-Fernández, Y. Martín, and J. Ruiz-Alzola, “Polyvinyl alcohol cryogel phantoms of biological tissues for wideband operation at microwave frequencies,” *PLoS ONE*, vol. 14, no. 7, pp. 1–17, 2019.
- [29] S. Di Meo *et al.*, “Tissue-mimicking materials for breast phantoms up to 50 GHz,” *Phys. Med. Biol.*, vol. 64, no. 5, 2019, Art. no. 55006.
- [30] D. Popovic *et al.*, “Precision open-ended coaxial probes for in vivo and ex vivo dielectric spectroscopy of biological tissues at microwave frequencies,” *IEEE Trans. Microw. Theory Tech.*, vol. 53, no. 5, pp. 1713–1722, May 2005.
- [31] “N1500A materials measurement suite features,” Keysight Technol., Santa Rosa, CA, USA, Rep., 2020. [Online]. Available: <https://www.keysight.com/de/de/assets/7018-04630/technical-overviews/5992-0263.pdf>
- [32] J. P. Dunsmore, *Handbook of Microwave Component Measurements: With Advanced VNA Techniques*. Hoboken, NJ, USA: Wiley, 2012.
- [33] M. T. Heideman, D. H. Johnson, and C. S. Burrus, “Gauss and the history of the fast Fourier transform,” *Archive Hist. Exact Sci.*, vol. 34, no. 3, pp. 265–277, 1985.
- [34] D. Seyfried and J. Schoebel, “Stepped-frequency radar signal processing,” *J. Appl. Geophys.*, vol. 112, pp. 42–51, Jan. 2015.
- [35] “LNF-LNR10_30A 10-30 GHz low noise amplifier,” Low Noise Factory, Göteborg, Sweden, Rep., 2017. [Online]. Available: https://www.lownoiseactory.com/files/9914/8978/3109/LNF-LNR10_30A.pdf
- [36] Council of the European Union European Parliament, “Directive 2004/40/EC of the European parliament and of the council of 29 April 2004 on the minimum health and safety requirements regarding the exposure of workers to the risks arising from physical agents (electromagnetic fields) (18th individual Directive within the meaning of Article 16(1) of Directive 89/391/EEC),” pp. 1–26, Apr. 2004. [Online]. Available: <https://eur-lex.europa.eu/legal-content/EN/ALL/?uri=CELEX:32004L0040>



DUY HAI NGUYEN received the B.Eng. and M.Eng. degrees in electrical engineering from Frankfurt University of Applied Sciences (FRA-UAS), Frankfurt, Germany, in 2012 and 2015, respectively. He is currently pursuing the Ph.D. degree with the Terahertz-Photonik Research Group, Goethe University Frankfurt, Frankfurt.

From 2016 to 2019, he was a Microwave Laboratory Engineer with FRA-UAS. His research focuses on millimeter-wave planar antenna designs for biomedical, and space applications.



JONATHAN STINDL received the B.Sc. degree in physics from Goethe University Frankfurt, Germany, in 2019, where he is currently pursuing the master's degree with the Atomic Physics Research Group. He is a Student Assistant with the Terahertz-Photonics Working Group, Goethe University Frankfurt.



TERESA SLANINA received the B.Sc. and M.Sc. degrees in biophysic from the Goethe University Frankfurt, Frankfurt, Germany, in 2020 and 2021, respectively.

She is currently a Research Assistant with the Terahertz-Photonik Research Group, Goethe University Frankfurt, Germany. Her research focusses on thermo-dielectric breast tissue phantoms for microwave technique and osteosynthesis-monitoring with electromechanical impedance technique.



JOCHEN MOLL (Member, IEEE) received the Dipl.Ing. and Ph.D. degrees in mechanical engineering from the University of Siegen, Siegen, Germany, in 2007 and 2011, respectively.

He is currently a Postdoctoral Research Assistant with Goethe University Frankfurt, Germany. His research interests include radar techniques for biomedical applications, signal processing and imaging techniques.



VIKTOR KROZER (Senior Member, IEEE) received the Dipl.Ing. and Dr.Ing. degrees in electrical engineering from the Technical University of Darmstadt (TU Darmstadt), Darmstadt, Germany, in 1984 and 1991, respectively.

In 1991, he became a Senior Scientist with TU Darmstadt, where he was involved in high-temperature microwave devices and circuits and submillimeter-wave electronics. From 1996 to 2002, he was a Professor with the Technical University of Chemnitz, Chemnitz, Germany.

From 2002 to 2009, he was a Professor of Electromagnetic Systems, DTU Elektro, Technical University of Denmark, Kongens Lyngby, Denmark, where he was heading the Microwave Technology Group. From 2009 to 2012, he was an endowed Oerlikon–Leibniz–Goethe Professor of Terahertz Photonics with Johann Wolfgang Goethe University, Frankfurt, Germany. Since 2012, he has been heading the Goethe–Leibniz–Terahertz Center. He is also with Ferdinand-Braun-Institut, Berlin, Germany, where he is leading the Terahertz Components and Systems Group. His current research interests include terahertz electronics and imaging, monolithic microwave integrated circuit, nonlinear circuit analysis and design, device modeling, biomedical sensors, and remote sensing instrumentation.



GERNOT ZIMMER received the Dipl.Ing. degree in electrical engineering from the University of Applied Sciences Trier in 1977, and the Dr.Ing. degree in electrical engineering from the Technical University Berlin in 1986.

From 1986 to 1988, he was a Research Assistant with AEG–Forschungsinstitut, Ulm, Germany. From 1989 to 1991, he served with the Telefunken Systemtechnik, Ulm, as a Staff Scientist. Since 1991, he has been a Professor and the Head of Microwave Engineering Laboratory with Frankfurt

University of Applied Sciences, Frankfurt, Germany. He has also been a Visiting Professor of RF–Engineering with Vietnamese German University, Ho Chi Minh, Vietnam, since 2009. He has authored the book *Hochfrequenztechnik—Lineare Modelle*.